

PHYSICOCHEMICAL STUDIES OF NICKEL DOPED ZnO NANOPARTICLES

Asghari Maqsood

Nano-scale Physics Laboratory,
Department of Physics,
Air University, Islamabad, Pakistan
Asghri.maqsood@mail.au.edu.pk; tpl.qau@usa.net

Iqra Sajid

Nano-scale Physics Laboratory,
Department of Physics,
Air University, Islamabad, Pakistan
miqra559@gmail.com

Aamir Mahmood

Nano-scale Physics Laboratory,
Department of Physics,
Air University, Islamabad, Pakistan
amk86@gmail.com

M. Saif Ullah Awan

Nanoscience and Technology Division,
National Centre for Physics,
Islamabad, Pakistan
sssawan@gmail.com

Mujtaba Ikram

Institute of Chemical Engineering and
Technology,
University of the Punjab, Lahore
mujtaba.icet@pu.edu.pk

Abstract

The physicochemical properties of zinc oxide (ZnO) nanoparticles (NPs) doped with nickel, $Zn_{1-x}Ni_xO$ ($x=0\%$, 2% , 4% , 6%) have been investigated. Thermal gravimetric analysis (TGA), powder x-ray diffraction (XRD), Fourier transform infrared (FT-IR), and ultra violet visible (UV-Vis) spectroscopy were used to characterize the samples, which were fabricated using the co-precipitation technique. The materialization of ZnO as well as its phase stability temperatures were determined using TGA. The formation of wurtzite and the substitution of Ni in the ZnO lattice were verified by powder XRD. With increasing Ni replacement, the average crystallite size decreased and ranged between 41 and 29 nm. The existence of vibrational modes at different energies revealed the modifications in ZnO nanostructures with Ni substitution using FT-IR spectroscopy. By increasing the Ni content in ZnO, UV-Vis spectroscopy confirmed that the bandgap decreases.

Keywords: Crystal structure; Nano particles; Optical materials and properties; X-ray techniques.

1. INTRODUCTION

Zinc oxide is a non-toxic, semiconductor-type material with tunable properties and chemical stability. It has a stable hexagonal wurtzite structure at ambient conditions [1, 2]. Because of fundamental chemistry and numerous applications of ZnO in capacitors, storage systems, and biosensors [3], their nanoparticles are important. The addition of Ni^{2+} to

nanostructured ZnO boosts AC conductivity by six to eight orders of magnitude, which is beneficial for solar cell applications [4]. Zinc oxide NPs (ZnO) are multifunctional and versatile materials that may be used in a variety of applications, including photovoltaic, electronics, thermo-electrics, neutron detection, biomedicine, and spintronics [5, 6]. ZnO NPs have excellent thermal and power stability, significant exciton binding energy (60 meV at RT), and a spectrum of absorption with a wide radiation range because of a direct bandgap of 3.3 eV. ZnO is a suitable candidate for solar cells and photo detectors because of its configurable absorption and emission properties in blue light/ ultraviolet, as well as its high electron mobility and carrier concentration [7]. ZnO can be used as a substrate and active material, passivation or an interfacial surface, an anti-reflection coating, or a photovoltaic module [8]. Absorption across a wide range of wavelengths is required to enhance the power conversion efficiency of solar cells. This needs materials with different bandgaps configured in a tandem array [7, 8].

As a result, modifying the bandgap of ZnO with the goal of improving solar cell performance is desired. Doping ZnO with transition metals (TMs) such as Fe, Cu, Mn, Co, and Ni allows for such bandgap tunability and, as a result, optical absorption shift [9]. Smaller bandgap ZnO-based materials are required in the applications of photo electrochemical (PEC) and solar cells and this is dependent on the use of synthesis process and type of dopant. The doping of ZnO with TM sources, Ni doping has the potential of shifting the optical bandgap to the region of red wavelengths [10]. Ni^{2+} is one of the most effective dopant TMs in ZnO

due to its chemical stability while inhibiting Zn^{2+} sites. The electrical and optical properties of ZnO improved due to unpaired electrons in Ni's d-orbitals, which have the ability of carrier's interactions [11]. The effect of Ni doping in ZnO is greatly influenced by the synthesis method employed. With increasing the Ni content from 2% to 15%, the bandgap of Ni-doped ZnO decreased from 3.43 to 2.87 eV, synthesized via spray pyrolysis deposition on quartz substrates [12]. Also, observed the reduction in the bandgap from 3.2 to 1.4 eV up to 7% of Ni-doped ZnO, fabricated by DC/RF magnetron-sputtering technique [13]. At the same time, the bandgap of Ni-doped ZnO NPs produced by the sol-gel method increased from 3.29 to 3.32 eV [14].

In this manuscript, the synthesis, thermal, structural, and optical properties of pure and Ni-doped ZnO NPs, demonstrating the structural transformation caused by Ni are reported.

The co-precipitation method was used to synthesize un-doped and doped Ni-ZnO NPs ($Zn_{1-x}Ni_xO$, $x = 0.00, 0.02, 0.04, \text{ and } 0.06$), following the previous reports [4, 15], and the sample fabrication steps are depicted in Fig. 1.



Fig. 1. Synthesis route for $Zn_{1-x}Ni_xO$ NPs.

A simultaneous thermal analyzer was used to perform the thermal analysis in the air atmosphere at a heating rate of $10\text{ }^\circ\text{C}$ per minute. A two-stage weight loss is indicated by a TGA transformation from $60\text{ }^\circ\text{C}$ to $550\text{ }^\circ\text{C}$, as shown in Fig. 2. Since the evaporation temperature of nitrates is about $130\text{ }^\circ\text{C}$, weight loss in the first stage is due to dehydration on zinc nitrate hydrate, where 2% weight loss occurs above the 102 to $165\text{ }^\circ\text{C}$ limits. In the second step, zinc nitrate hydrate decomposes into zinc oxide, resulting in a 7.5% weight loss before $310\text{ }^\circ\text{C}$. Although the decomposition of nitrate ions begins at $312\text{ }^\circ\text{C}$, nitrogen peroxide, as well as a line attributed to the N_2O^4 radical, can be seen at temperatures ranging from 240 to $550\text{ }^\circ\text{C}$. Up to $310\text{ }^\circ\text{C}$, an absolute weight loss of 9.5% occurs; after this temperature, no significant

weight loss occurs. The temperature at which ZnO achieves phase stability is $310\text{ }^\circ\text{C}$. This finding is consistent with previous research [16-18].

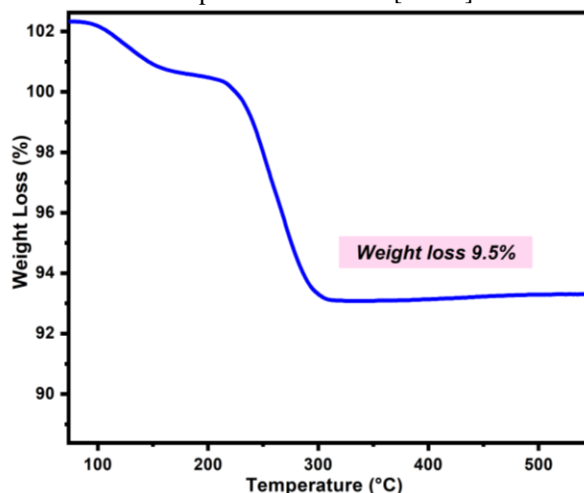


Fig. 2. TGA trace of pure ZnO NPs.

An X-ray diffractometer with $CuK\alpha$ ($\lambda = 1.5406\text{ \AA}$) was used to perform X-ray diffraction (XRD) of the annealed samples at room temperature. Fig. 3a shows the indexed XRD patterns of all the samples. JPCDS card no. 89-1397 matches with all the peaks perfectly. The indexed patterns correspond to reflections from the hexagonal wurtzite structure of ZnO [19, 20]. The diffraction patterns of $Zn_{1-x}Ni_xO$ for $x = 0.02, 0.04, \text{ and } 0.06$, display XRD characteristic lines like those for un-doped ZnO NPs where Zn atoms are partially replaced by Ni atoms in the crystal lattice and conform the single-phase hexagonal wurtzite structure of ZnO is preserved for all the Ni substitutions. Fig. 3b shows an enlarged view of the peaks shifting towards the higher diffracting angle in the XRD characteristic lines for $Zn_{1-x}Ni_xO$ NPs ($x = 0.00, 0.02, 0.04, \text{ and } 0.06$), demonstrating the non-uniform stresses generated in ZnO. As a result of XRD analysis, slight changes in the values of lattice constants can be predicted and estimated using standard relations [21]. The a and c values decrease slightly when Ni is substituted in the $Zn_{1-x}Ni_xO$ lattice due to the smaller ionic radius [22] of Ni^{2+} (0.69 \AA) compared to Zn^{2+} (0.74 \AA), but the c/a ratio remains nearly the same. The average crystallite sizes for nickel-doped ZnO nanostructures estimated by the Scherrer equation [21] range from 41 to 29 nm ; the decrease in crystallite size is due to the mismatch of Ni^{2+} and Zn^{2+} ionic radii [16]. The specific surface area [22] increases as the crystallite size decreases. The values of various parameters corresponding to different concentrations of Ni substituted in ZnO are tabulated in Table 1.

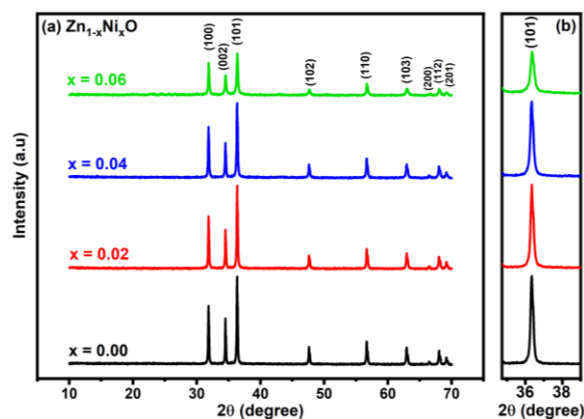


Fig. 3. (a) X-ray diffraction patterns (b) Enlarged view of the (101) peak shifting for Zn_{1-x}Ni_xO nanostructures.

FT-IR measurements have further confirmed the formation of the Wurtzite structure of Zn_{1-x}Ni_xO. FT-IR spectra observed in the 400- 4000 cm⁻¹ are shown in Fig. 4. The band around 522 to 505cm⁻¹ corresponds to the vibrational energies of zinc oxide bonds that may have hexagonal vibration mode characteristics, indicating that ZnO was formed [4, 23]. By comparing the FT-IR spectra of pure and Ni-doped ZnO nanostructures, the effect of Ni doping on structural modification of ZnO nanostructures was investigated. The Ni-O bond is detected with a peak at 625 cm⁻¹ in 6 % Ni-doped ZnO spectra, suggesting active Ni substitution in ZnO lattices, which is due to vibrations of Zn-O-Ni local bonds and modes from defect states, which involves increased Ni substitution in ZnO [15]. The vibrations of C-O stretching due to the accumulation of carbon monoxide from moisture in samples are represented by the band at 1099-1086 cm⁻¹ [24]. The peaks at 1618 and 1648 cm⁻¹ for 4 % and 6 % Ni-doped ZnO are associated with O-H bending vibrations of water molecules (H₂O), a small amount of moisture in ZnO NPs. H-bonded O-H stretching can be seen in the 3428 to 3471 cm⁻¹ zone [25].

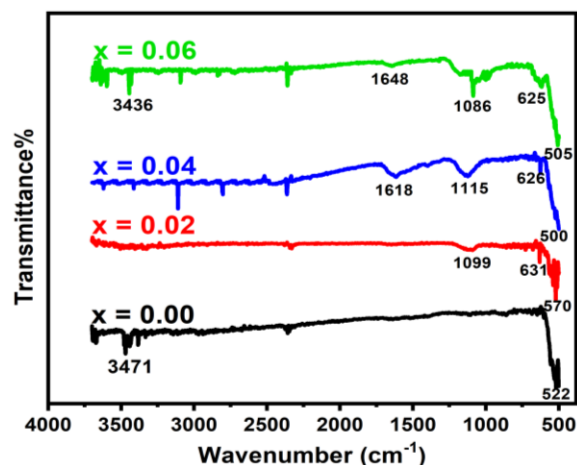
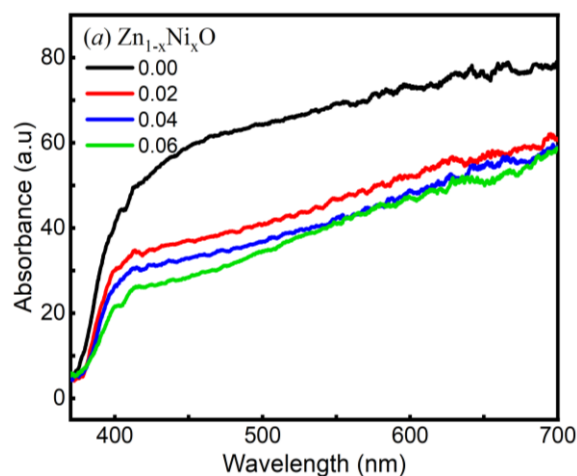


Fig. 4. FT-IR spectra for Zn_{1-x}Ni_xO NPs.

The diffused reflectance distribution of ZnO and Zn_{1-x}Ni_xO is shown in Fig. 5a. When Ni is substituted, the signature shoulder becomes red-shifted, implying a reduction in the bandgap [18]. The narrowing of the band edge also indicates that Ni has been incorporated into the ZnO crystal structure [19, 20]. Gao et al. [18] found the same redshift in Ni-doped ZnO. As Ni is incorporated, the reflectance edge redshifts, which may be due to the formation of a faulty Ni energy level. Zn causes a shallow donor level below the conduction band as a donor impurity, lowering the bandgap of ZnO.



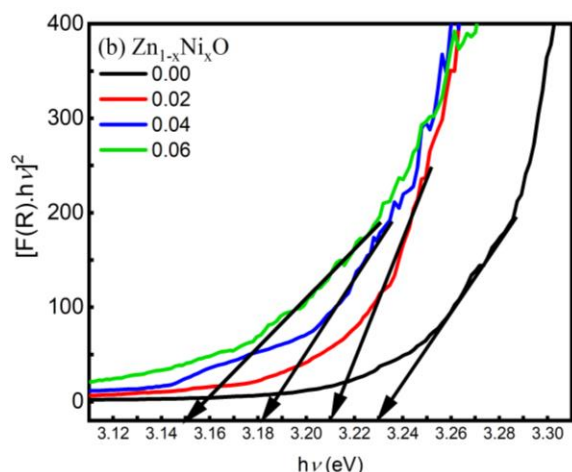


Fig. 5. (a) Reflectance as a function of wavelength at

room temperature (b) Tauc plots as a function of energy for different concentration of Ni in ZnO. The bandgap decreased from 3.23 eV to 3.15 eV as Ni concentration increased, as tabulated in Table 1. The decrease in bandgap may be attributable to sp-d exchange interactions of substituted divalent ions between band electrons and localized d electrons [15].

Table 1. Lattice constants, c/a ratio, average crystallite size, density, specific surface area, FT-IR data and optical bands of $Zn_{1-x}Ni_xO$.

Composition (x)	0%	2%	4%	6%
Lattice constant, a (Å)	3.24(±1)	3.241(±1)	3.24(±1)	3.23(±1)
Lattice constant, c (Å)	5.19(±1)	5.19(±1)	5.19(±1)	5.18(±1)
c/a ratio	1.602	1.602	1.602	1.602
Volume (Å ³)	47.30	47.22	47.11	46.94
Crystallite size (nm)	41	38	36	29
Density (g/cm ³)	5.72(±1)	5.716	5.72	5.75
Specific surface area(m ² /g)	25.38	27.50	28.89	35.95
Zn-O bond (cm ⁻¹)	522	570	500	505
Ni-O bond (cm ⁻¹)	-	631	626	625
C-O bond (cm ⁻¹)	-	1099	1115	1086
H-O-H bond (cm ⁻¹)	-	-	1618	1648
O-H bond (cm ⁻¹)	3428	-	-	3436
Bandgap (eV)	3.23	3.21	3.18	3.15

It is concluded that the co-precipitation method was used to prepare $Zn_{1-x}Ni_xO$ ($x = 0, 2, 4, 6\%$) samples successfully. Thermo-gravimetric analysis indicates that 310°C is the phase stability temperature for zinc nitrate hydrate decomposition into zinc oxide. All the samples have the hexagonal wurtzite form with a slight peak shifting in the diffraction angle with doping of Ni are established from the XRD analysis. The crystallite size decreases as the Ni content in the ZnO lattice increases. The formation of the ZnO phase and Ni²⁺ substitution is confirmed by the absorption

peaks at 522 and 625cm⁻¹ in FT-IR analysis. The optical bandgap narrowed as the concentration of Ni increased in the samples.

NOMENCLATURE

ZnO	Zinc Oxide
Zn	Zinc
Ni	Nickel
O	Oxygen
TGA	Thermal Gravimetric Analysis

XRD	x-ray diffraction
FT-IR	Fourier Transform Infrared
UV-Vis	Ultra Violet visible
NP	Nanoparticle
AC	Alternate current
RT	Room Temperature
eV	Electronic Volt
TM	Transition Metals
Cu	Copper
Mn	Manganese
Co	Cobalt
Fe	Iron
α	Alpha
λ	Lamda (wave length)
Å	Angstrom
H	Hydrogen
H ₂ O	Water

ACKNOWLEDGEMENTS

The author A. Maqsood is thankful to the Pakistan Academy of Sciences for funding this project. Dr M. Nawaz Khan is acknowledged for helpful discussion. Syed Ikram Naqvi is thanked for checking the references and critical reading.

REFERENCES

- [1] Z. Fan, J. G. Lu, *J. Nanosci. Nanotechnol.* vol. 5, no. 10, pp. 1561-1573, 2005.
- [2] D. Sharma, S. Sharma, B.S. Kaith, J. Rajput, M.J Kaur, *Appl. Sur. Sci.* vol. 257, no.22 pp. 9661-9672, 2011.
- [3] I. Abood, *J. Nanotech. Mater.* vol. 4, no.1, pp. 1-8, 2017.
- [4] N. Goswami, A. Sahai, *Mat. Res. Bull.* vol. 48, no. 2, pp. 346-351, 2013.
- [5] Y. Wang, C. Zhou, A.M. Elquist, A. Ghods, V.G. Saravade, N. Lu, I. Ferguson, *Proceedings Vol 10533, Oxide-based Materials and Devices IX*, 105331R, 2018.
- [6] A. Kołodziejczak-Radzimska, T. Jesionowski, *Materials*, vol. 7, pp. 2833-2881, 2014.
- [7] B. Hussain, A. Ebong, I.J.S.E.M. Ferguson, *Solar Energy Materials and Solar Cells*, vol. 139, pp. 95-100, 2015.
- [8] T.M. Razykov, C.S. Ferekides, D. Morel, E. Stefanakos, H.S. Ullal, H.M. Upadhyaya, *Materials Sciences and Applications*, vol. 85, no. 8, pp. 1580-1608.
- [9] D.P. Joseph, Venkateswaran, *Journal of Atomic, Molecular, and Optical Physics* vol. 2011 pp. 270540-7, 2011.
- [10] H. Ali, A. Alsmadi, B. Salameh, M. Mathai, M. Shatnawi, N. Hadia, E.J. brahim, *J. Alloys. Compd.* vol. 816, pp. 152538, 2020.
- [11] S.C. Das, R.J. Green, J. Podder, T.Z. Regier, G.S. Chang, *J. Phy. Chem C*, vol. 117 no. 24 pp. 12745-12753, 2013.
- [12] G.K. Mani, J.B.B. Rayappan, *Superlattices and Microstructures*, vol. 67, pp. 82-87, 2014.
- [13] R. Elilarassi, G.J. Chandrasekaran, *J. Mater. Sci: Mater Electron* vol. 22, no.7, pp. 751-756, 2011.
- [14] M. Ali, S. Sharif, S. Anjum, M. Imran, M. Ikram, M. Naz, S. Ali, *Mater. Res. Express*, vol.6, no. 12, pp. 1250d5, 2020.
- [15] R. Chauhan, A. Kumar, R. Chaudhary, *J. Optoelectron. Biomed. Mater.*, vol. 3 no. 1, pp. 17-23, 2020.
- [16] S. Fabbiyola, V. Sailaja, L.J. Kennedy, M. Bououdina, J.J. Vijaya, *J. Alloys Compd.*, vol 694, pp. 522-531, 2017.
- [17] A.K. Arora, S. Devi, V.S. Jaswal, J. Singh, M. Kinger, V.D. Gupta, *Orient J Chem* vol. 30, no. 4, pp. 1671-1679, 2014.
- [18] R. Saravanan, K. Santhi, N. Sivakumar, V. Narayanan, A. Stephen, *Materials Characterization*, vol. 67, pp. 10-17, 2012.
- [19] J. Xu, M. Li, L. Yang, J. Qiu, Q. Chen, X. Zhang, Y. Feng, J.. Yao, *Chemical Engineering Journal* vol. 394, pp. 125050, 2020.
- [20] G. Srinet, R. Kumar, V. Sajal, *J. Appl. Phys.*, vol. 114, no. 3, pp. 033912.
- [21] H. Khan, A.S. Yerramilli, A. D'Oliveira, T.L. Alford, D.C. Boffito, G.S. Patience, *The Canadian Journal of Chemical Engineering*, vol. 98, no. 6, pp. 1255-1266, 2020.
- [22] M. Arshad, A. Maqsood, I. H. Gul, M. Anis-Ur-Rehman, *Mater. Res. Bull.*, vol 87, pp. 177-185, 2017.

- [23] G. Vijayaprasath, R. Murugan, S. Palanisamy, N. M. Prabhu, T. Mahalingam, Y. Hayakawa, G. Ravi, *Mater. Res. Bull.*, vol. 76, pp. 48-61, 2016.
- [24] R.S. Kumar, S. H. S. Dananjaya, M. De Zoysa, M. Yang, *RSC Advances*, vol. 6, no. 110, pp. 108468-108476, 2016.
- [25] G. Srinet, R. Kumar, V. Sajal, *Journal of Appl. Phys.*, vol. 114 no.3, pp. 033912, 2013.